# Philosophical Magazine A

# Accurate atomistic simulation of (a/2) ⟨111⟩ screw dislocations and other defects in bcc tantalum

L. H. Yang [a] , P. Söderlind [a] & J. A. Moriarty [a]

[a] Physics and Advanced Technologies Directorate, Lawrence
Livermore National Laboratory , University of California ,
Livermore, California, 94551, USA
Published online: 05 Aug 2009.

PLEASE SCROLL DOWN FOR ARTICLE

# Accurate atomistic simulation of $(a/2)\langle 111 \rangle$ screw dislocations and other defects in bcc tantalum

L. H. YANG†, PER SÖDERLIND and JOHN A. MORIARTY

Physics and Advanced Technologies Directorate, Lawrence Livermore National Laboratory, University of California, Livermore, California 94551, USA

## ABSTRACT

The fundamental atomic-level properties of $(a/2)\langle 111 \rangle$ screw dislocations and other defects in bcc Ta have been simulated by means of new quantum-based multi-ion interatomic potentials derived from the model generalized pseudopotential theory (MGPT). The potentials have been validated in detail using a combination of experimental data and *ab-initio* electronic structure calculations on ideal shear strength, vacancy and self-interstitial formation and migration energies, grain-boundary atomic structure and generalized stacking-fault energy ($\gamma$) surfaces. Robust and accurate two- and three-dimensional Green's function (GF) techniques have been used to relax dynamically the boundary forces during the dislocation simulations. The GF techniques have been implemented in combination with a spatial domain decomposition strategy, resulting in a parallel MGPT atomistic simulation code that increases computational performance by two orders of magnitude. Our dislocation simulations predict a degenerate core structure with threefold symmetry for Ta, but one that is nearly isotropic and only weakly polarized at ambient pressure. The degenerate nature of the core structure leads to possible antiphase defects (APDs) on the dislocation line as well as multiple possible dislocation kinks and kink pairs. The APD and kink energetics are elaborated in detail in the low-stress limit. In this limit, the calculated stress-dependent activation enthalpy for the lowest-energy kink pair agrees well with that currently used in mesoscale dislocation dynamics simulations to model the temperature-dependent single-crystal yield stress. In the high-stress limit, the calculated Peierls stress displays a strong orientation dependence under pure shear and uniaxial loading conditions, with an antitwinning–twinning ratio of 2.29 for pure shear $\{211\}$–$\langle 111 \rangle$ loading.

## § 1. INTRODUCTION

In the development of modern materials theory and simulations, there is a growing need for a fundamental understanding and reliable description of lattice defects and their properties, including dislocations, grain boundaries and point defects. In particular, most mechanical properties of metals are directly affected by the presence of dislocations and the interaction between them, and any predictive theory of crystal plasticity must accurately describe their behaviour. In many situations, of course, dislocation behaviour is dominated by the elastic strain field, which for

---

† Email: lyang@llnl.gov

distances more than a few atomic spacings from the centre of the dislocation is well described by linear continuum elasticity. However, such a continuum description does not account for short-range nonlinear core effects and the intrinsic dislocation–lattice coupling, which for $(a/2)\langle 111\rangle$ screw dislocations in bcc metals are responsible for the observed anisotropic crystal plasticity (Duesbery *et al.* 1973, Vitek 1976, Duesbery and Vitek 1998), as well as the strong temperature dependence of the yield stress (Duesbery 1983a, b, Duesbery and Basinski 1993). Therefore an accurate and detailed description of dislocation properties on the atomic scale has become increasingly important both to advance modern dislocation theory and to develop predictive multiscale simulations of crystal plasticity in these materials.

Accurate atomistic simulation of dislocation behaviour in bcc metals involves a number of important physical and computational issues. In addition to treating the strong short-range core effects, an atomistic simulation of dislocation behaviour must account for the long-range elastic field generated by the extended dislocation itself. In general, this can be accomplished by using sufficiently remote fixed-boundary conditions, where the atomic positions at the outer regions of the simulation cell are fixed by anisotropic linear elasticity. In fact, most atomistic simulations of singledislocation properties reported in the literature have been performed with this type of boundary condition. However, with fixed-boundary conditions, important details such as the incompatability between fixed and fully relaxed atomistic regions, simulation-cell size effects and restrictions on the dislocation geometry can have a large influence on the dislocation properties under study (Rao *et al.* 1998). Another important issue in the atomistic simulation of dislocations and other lattice defects in bcc transition metals is how to describe the forces between atoms in both an accurate and tractable manner. Although empirical radial-force interatomic potentials of either the Finnis–Sinclair (FS) (1984) type or the embedded-atom model (EAM) type (Daw and Baskes 1983) are now often used and are computationally very efficient, such potentials are only fully justified for metals with closed or nearly closed d-electron shells, such as the fcc noble metals. For bcc transition metals with partially filled d bands, directional bonding is present that gives rise to nonradial forces and the need for explicit angular-force contributions to the interatomic potentials (Moriarty 1988, Carlsson 1990, Pettifor *et al.* 1995). These contributions are found to be generally important to the structural and mechanical properties of the bcc metals; so it is highly desirable to include them.

In recent years, quantum-based interatomic potentials for bcc transition metals that contain explicit angular-force contributions have been developed both from tight-binding theory (Carlsson 1991, Foiles 1993, Pettifor *et al.* 1995) and from first-principles generalized pseudopotential theory (GPT) (Moriarty 1988). The latter include the model generalized pseudopotential theory (MGPT) potentials of Moriarty (1990a, b, 1994) which have been systematically derived from the firstprinciples theory. Many-body angular forces are accounted for in the MGPT through explicit analytic three- and four-ion potentials. While MGPT potentials can provide the desired physical accuracy, they are necessarily much more computationally intensive than short-range radial-force FS or EAM potentials; so simulation-cell size can become an issue in large-scale applications. In particular, previous three-dimensional (3D) simulations of screw dislocations in bcc Mo with MGPT potentials and fixed-boundary conditions (Xu and Moriarty 1996, 1998) showed that the simulation-cell size must be very large (about 100 000 atoms) to avoid a force build-up around the boundary between fixed and relaxed atomistic regions.

To overcome the problems with fixed-boundary conditions, Rao *et al.* (1998) have recently developed new Green's-function (GF) based flexible-boundary conditions. Their approach builds on the earlier two-dimensional (2D) methods of Sinclair *et al.* (1978) and others and provides robust flexible-boundary conditions for both 2D and 3D simulations. In this technique, a buffer layer is introduced between the outer fixed and inner relaxed atomistic regions that allows one to update dynamically the boundary conditions of the simulation, while dramatically decreasing the size of the inner atomistic region. Using their scheme, Rao *et al.* were able to perform 3D EAM simulations of dislocation kink-pair structures with about 90% reduction in the number of atoms in the inner atomistic region, while maintaining the same level of accuracy as with fixed-boundary conditions. In present work, we have developed advanced MGPT interatomic potentials for bcc Ta and implemented them in 2D and 3D atomistic simulations using the Rao *et al.* flexible-boundary conditions to study fundamental dislocation properties of this metal. Our new atomistic MGPT simulation code combines the GF-based flexible-boundary conditions with a spatial domain decomposition technique to calculate optimized dislocation structures in the presence of an arbitrary stress with an overall increase in computational speed of at least two orders of magnitude. We are thereby able to simulate a wide range of $(a/2)\langle 111 \rangle$ screw dislocation properties for Ta in an accurate and highly efficient manner.

More generally, we are interested in understanding and simulating dislocation mobility in bcc metals under a wide variety of stress and temperature conditions. Such information represents important input into higher-length-scale descriptions of plasticity at both ambient and extreme conditions and is explicitly required in modern mesoscale dislocation dynamics simulations (Tang *et al.* 1998). Towards this end, we have developed, validated and applied MGPT potentials for Ta over a very large pressure range, extending to 1000 GPa (10 Mbar). Brief preliminary accounts of some of this work have appeared elsewhere (Yang and Moriarty 2000, Yang *et al.* 2000). In this paper, we shall focus on a full detailed report of our results at or near ambient conditions. In addition to our dislocation simulations, we have also considered several other selected deformation and defect properties as relevant validation tests of the MGPT potentials. In this regard, our development and validation of the present Ta potentials has made extensive use of *ab-initio* electronic structure calculations of basic structural, vibrational, mechanical and defect properties of the bulk metal (Söderlind and Moriarty 1998, Söderlind *et al.* 2000). These calculations have here been supplemented with additional *ab-initio* results on ideal shear strength, point-defect formation and migration energies, and the generalized stacking-fault energy ($\gamma$) surfaces. The extension of the present dislocation studies to high pressure will be presented elsewhere (Yang *et al.* 2001).

Whether at ambient or extreme pressure, it is expected that the low-temperature and high-strain-rate plastic deformation properties of bcc metals are controlled by intrinsic core properties of the $(a/2)\langle 111 \rangle$ screw dislocations. In particular, the stress-dependent core configuration on the atomic scale plays an important role in constraining the motion of dislocations overcoming the Peierls barrier (Duesbery 1984a, b, Suzuki *et al.* 1991) and in the interaction of dislocations at close distances. In general, the unstressed bcc dislocation core is expected to display a nonplanar configuration with either threefold symmetry and doubly degeneracy (Vitek 1974, Suzuki *et al.* 1991, Xu and Moriarty 1996, Duesbery and Vitek 1998) or else sixfold symmetry and nondegeneracy (Duesbery and Vitek 1998, Ismail-Beigi and Arias 2000). As we shall demonstrate here, the two cases are, in fact, closely related

through the pressure-dependent polarization of the core, which exactly vanishes for the latter sixfold-symmetric configuration. At ambient conditions we predict a very weakly polarized core for Ta, but one that is subject to rapid change depending on the precise volume and pressure conditions.

At low temperatures, the motion of the $(a/2)\langle 111 \rangle$ screw dislocation is believed to be associated with the formation of mobile kinks on the dislocation line. Because kink properties are closely linked to the core structure, the nucleation and motion of kink pairs under stress can be complex (Duesbery 1983a, b, M. S. Duesbery 1999, unpublished, Yang and Moriarty 2000, Rao and Woodward 2001). Here we elaborate the expected kink and kink-pair energetics for the weakly polarized Ta core in the low-stress limit. Another important intrinsic core property associated with the dislocation motion is the zero-temperature Peierls stress required to move the infinite straight screw dislocation, as measured by the critical resolved shear stress (CRSS). For bcc metals, it is expected that there is a strong dependence of the CRSS on the orientation of the applied glide stress (Duesbery 1984a, b, Ito and Vitek 2001). Moreover, it has been argued that the degree of the orientation dependence of the CRSS is governed by special features of the screw dislocation cores (Suzuki *et al.* 1991). Here we shall examine the Peierls stress of Ta under various representative loading conditions involving both pure shear and shear plus uniaxial stress components.

The remainder of this paper is organized as follows. In §2 we discuss the details of our computational approach, including the use of *ab-initio* electronic structure methods, the present MGPT potentials for Ta, and our new GF atomistic simulation technique for dislocation calculations. Validation of the Ta MGPT potentials with available experimental data and new *ab-initio* electronic structure calculations on selected deformation and defect properties will be discussed in §3, together with an elaboration of $\gamma$ energy surfaces for the $\{110\}$ and $\{211\}$ slip planes. Our atomistic dislocation simulation results for Ta on core structure, kink and kink-pair energetics, and the Peierls stress and its orientation dependence are presented in §4. We conclude in §5.

## §2. COMPUTATIONAL APPROACH

### 2.1. *Full-potential linear muffin-tin orbital and pseudopotential electronic structure methods*

The present section briefly summarizes the details of our *ab-initio* electronic structure methods used in the this work, which include both full-potential (FP) linear muffin-tin orbital (LMTO) and pseudopotential (PP) techniques. The FP LMTO method has been used previously to study basic structural, vibrational and mechanical properties in Ta to 1000 GPa (10 Mbar) (Söderlind and Moriarty 1998). The FP LMTO and PP methods were also used previously to study vacancy formation in bcc metals, including Ta (Söderlind *et al.* 2000). The FP LMTO results have been directly employed here in the development of our present Ta MGPT potentials, as described below in §2.2. To validate further the potentials, entirely new *ab-initio* results have been obtained on the ideal shear stress, vacancy migration, self-interstitial formation and migration, and high-symmetry features of the $\{110\}$ and $\{211\}$ $\gamma$ surfaces.

Our FP LMTO and PP methods are implemented within first-principles density functional theory (Hohenberg and Kohn 1964, Kohn and Sham 1965) and require only the atomic number (73 for Ta) and an assumed functional form for the

exchange and correlation energy of the electrons as input. This latter functional has been treated both within the standard local-density approximation (LDA) (Kohn and Sham 1965) and the more recent generalized gradient approximation (GGA) of Perdew *et al.* (1992). In general, we have found that the GGA is the more accurate of the two approaches for Ta, and our FP LMTO calculations have used this treatment, except as noted. In both our FP LMTO and our PP approaches, the electron charge density and potential are allowed to have any geometrical shape and are calculated self-consistently. In our FP LMTO approach, we incorporate non-sphericity to the charge density and potential by representing the crystal with non-overlapping spheres (of a variable optimum size) surrounding each atomic site and a general shaped interstitial region between the spheres. Inside the spheres, the wavefunctions are represented as Bloch sums of LMTOs and are expanded by means of structure constants. The kinetic energy is not restricted to be zero in the interstitial region and the wavefunction expansion contains Hankel or Neumann functions (depending on sign of the kinetic energy) together with Bessel functions. Also in our FP LMTO method, all relativistic terms, including the spin-orbit coupling, are included in the Hamiltonian. In order to represent the wavefunctions in Ta as accurately as possible we have treated 5s, 5p and 4f semicore states on the same footing as the 6s, 6p, 5d and 5f valence states. In addition, the numerical basis set used is extended to a so-called double basis set in order to minimize truncation errors in the expansion of the wave functions (Söderlind and Moriarty 1998).

The role of the *ab-initio* PP calculations in the present work is twofold. First, they provide relaxed configurations for subsequent FP LMTO calculations on the vacancy migration energy and the $\gamma$ surfaces, in the same manner as done previously for the vacancy formation energy (Söderlind *et al.* 2000). Second, the PP method is used to perform additional relaxed calculations of self-interstitial formation and migration energies. Söderlind *et al.* (2000) previously found that FP LMTO GGA and FP LMTO LDA vacancy formation energies are the same in Ta; so all the present point-defect calculations have been performed with a somewhat simpler semirelativistic LDA treatment. All remaining FP LMTO calculations have been done with the fully relativistic GGA treatment. The FP LMTO results reported here have been obtained with the latest version of computer code developed by J. M. Wills (2000, unpublished) while the PP results reported have employed the parallel code developed by Yang (1999).

### 2.2. *Model generalized pseudopotential theory interatomic potentials*

The present dislocation calculations on Ta have been carried out using quantum-based multi-ion interatomic potentials derived from the MGPT (Moriarty 1990a, 1994). This approach is based on the corresponding first-principles GPT for transition metals developed directly from density functional theory (Moriarty 1988). The latter provides a rigorous real-space expansion of the total energy for the bulk metal in the form

$$E_{\text{tot}}(\mathbf{R}_1, \ldots, \mathbf{R}_N) = NE_{\text{vol}}(\Omega) + \tfrac{1}{2}{\sum_{i,j}}' v_2(ij;\, \Omega) + \tfrac{1}{6}{\sum_{i,j,k}}' v_3(ijk;\, \Omega)$$

$$+ \tfrac{1}{24}{\sum_{i,j,k,l}}' v_4(ijkl;\, \Omega), \tag{1}$$

where $\mathbf{R}_1, \ldots, \mathbf{R}_N$ denotes the positions on the $N$ ions in the metal, $\Omega$ is the atomic volume, and the prime on each sum over ion positions excludes all self-interaction terms where two indices are equal. The leading volume term $E_{vol}$ in his expansion as well as the two-, three- and four-ion interatomic potentials, $v_2, v_3$ and $v_4$ respectively, are volume-dependent but *structure-independent* quantities and are thus *transferable* to all bulk ion configurations. The angular-force multi-ion potentials $v_3$ and $v_4$ reflect contributions from partially filled d bands and are generally important for central transition metals. Within the MGPT framework, these potentials are systematically approximated by introducing canonical d bands and other simplifications to achieve short-ranged analytic forms, which can then be applied to both static and dynamic simulations, including the present dislocation simulations performed with the GF techniques described below. To compensate for the approximations introduced into the MGPT, a limited amount of parametrization is allowed in which the volume-dependent coefficients of the modelled potential contributions are constrained by experimental or *ab-initio* theoretical data. In this regard, the previous parametrization schemes developed for Mo (Moriarty 1990a, 1994) and Nb (Moriarty 1990b) have been generalized and improved, as we now describe for the present case of Ta.

In the MGPT, the radial-force two-ion pair potential $v_2$ in equation (1) is obtained as a sum of simple-metal sp hard-core overlap and tight-binding-like d-state contributions:

$$v_2(r; \Omega) = v_2^{sp}(r; \Omega) + v_2^{hc}(r; \Omega) + v_2^{d}(r; \Omega). \tag{2}$$

In equation (2) the simple-metal potential $v_2^{sp}$ and the hard-core potential $v_2^{hc}$ are retained directly from the first-principles GPT, while the d-state potential $v_2^{d}$ is developed in the form

$$v_2^{d}(r; \Omega) = v_a(\Omega)[f(r)]^4 - v_b(\Omega)[f(r)]^2, \tag{3}$$

where $f(r)$ is the radial component of the tight-binding-like d–d matrix element linking two ions, and $v_a$ and $v_b$ are volume-dependent coefficients. For pure canonical d bands, $f(r) \sim r^{-5}$, but in the MGPT this is generalized to include an $r^{-p}$ radial dependence. In addition, a new and smoother Gaussian cut-off of $f(r)$ beyond a specified radius $R_0$ is now included in the present treatment:

$$f(r) = \begin{cases} \left(\dfrac{r_0}{r}\right)^p, & r < R_0, \\[2ex] \left(\dfrac{r_0}{r}\right)^p \left[1 + \alpha\left(\dfrac{r}{R_0} - 1\right)^2\right] \exp\left[-\alpha\left(\dfrac{r}{R_0} - 1\right)^2\right], & r > R_0. \end{cases} \tag{4}$$

Here $r_0 = 1.8 R_{WS}$, with $R_{WS}$ the Wigner–Seitz radius, $R_0 = 2.15 R_{WS}$ and $\alpha = 75$. The latter values of $R_0$ and $\alpha$ ensure that $f(r)$ is negligible beyond second-neighbour distances in the bcc structure, while the functional form of equation (4) ensures that $f(r)$ and its first three derivatives are continuous across $R_0$. In the present application to Ta the power $p$ is allowed to be weakly volume dependent with a value of $p = 4$ near ambient conditions, as previously adopted for Mo (Moriarty 1990a, 1994) and Nb (Moriarty 1990b).

The angular-force three- and four-ion potentials, $v_3$ and $v_4$ respectively, are the appropriate multi-ion generalizations of $v_2^{d}$. At a given volume $\Omega$, the potential $v_3$ is a 3D function of the separation distances $r_1, r_2,$ and $r_3$ linking three ions, given by

$$v_3(r_1, r_2, r_3; \Omega) = v_c(\Omega)f(r_1)f(r_2)f(r_3)L(\theta_1, \theta_2, \theta_3) + v_d(\Omega)\{[f(r_1)f(r_2)]^2 P(\theta_3)$$
$$+ [f(r_2)f(r_3)]^2 P(\theta_1) + [f(r_3)f(r_1)]^2 P(\theta_2)\}, \qquad (5)$$

while the potential $v_4$ is a six-dimensional function of the six separation distances linking four ions, given by

$$v_4(r_1, r_2, r_3, r_4, r_5, r_6; \Omega) = v_e(\Omega)[f(r_1)f(r_2)f(r_4)f(r_5)M(\theta_1, \theta_2, \theta_3, \theta_4, \theta_5, \theta_6)$$
$$+ f(r_3)f(r_2)f(r_6)f(r_5)M(\theta_7, \theta_8, \theta_9, \theta_{10}, \theta_5, \theta_{12})$$
$$+ f(r_1)f(r_6)f(r_4)f(r_3)M(\theta_{11}, \theta_{12}, \theta_5, \theta_6, \theta_3, \theta_4)], \qquad (6)$$

where $v_c, v_d$ and $v_e$ are additional volume-dependent coefficients. The quantities $L$, $P$ and $M$ in equations (5) and (6) are universal angular functions which depend only on d symmetry and apply to all transition metals and all volumes. These functions have exact analytic representations which have been given by Moriarty (1990).

The five d state coefficients $v_a, v_b, v_c, v_d$ and $v_e$ in equations (3), (5) and (6) are material parameters that depend primarily on d-band filling and width. These quantities together with the volume term $E_{vol}$ are used to constrain the total energy and the multi-ion potentials. As a function of volume, these quantities are here fitted to theoretical and experimental data on the bcc equation of state, unrelaxed vacancy formation energy, shear elastic moduli and Debye temperature, under the additional constraint of the so-called compressibility sum rule (Pines and Noziéres 1966). The latter ensures that the bulk modulus calculated from volume derivatives of the total energy agrees with that calculated in the long-wavelength limit from position derivatives of the potentials. The constraining physical data for Ta have been obtained from our *ab-initio* FP LMTO results (Söderlind and Moriarty 1998, Söderlind *et al.* 2000), as slightly modified to maintain exact agreement with experiment near ambient conditions. We have so generated Ta potentials over a wide volume range and up to 1000 GPa in pressure. In the present context, the most notable uncertainty in this procedure is the value assigned to the unrelaxed vacancy formation energy $E_{vac}^0$. This quantity has an effective (experimental) uncertainty of about 0.3 eV (10%) at ambient pressure and has spawned several closely related sets of Ta MGPT potentials. The present potentials, which we label Ta-IV, assign a value $E_{vac}^0 = 3.20$ eV at the observed (300 K) equilibrium volume $\Omega_0 = 121.6$ au. This value appears to be near optimum for describing the ambient-pressure defect and deformation properties of interest here.

A few selected bulk properties of Ta calculated at $\Omega = \Omega_0$ with the present MGPT potentials are listed in table 1 and compared with both experimental data (Woods 1964, Kittel 1976, Katahara *et al.* 1979) and *ab-initio* FP LMTO results (Söderlind and Moriarty 1998, Söderlind *et al.* 2000). Included are the six specific quantities constraining the potentials at this volume, plus pressure derivatives of the bulk and elastic moduli, structural energy differences and some representative phonon properties. The pressure derivatives are accurately maintained by fitting the bulk and shear elastic moduli as a function of volume. The bcc structure itself is predicted to be the lowest energy stable phase at all volumes considered, although the open-packed A15 structure is competitive at large volumes. While the fcc–bcc and A15–bcc energy differences are somewhat underestimated for Ta in the present MGPT treatment compared with the FP LMTO results, the trends with both structure and volume are well described. Phonon frequencies are typically calculated to an accu-

Table 1.   Bulk properties of bcc Ta: cohesive energy $E_{\mathrm{coh}}$, *unre-laxed* vacancy formation energy $E_{\mathrm{vac}}^0$, bulk modulus $B$, shear elastic moduli $C_{44}$ and $C'$, phonon frequencies $L, T_1$ and $T_2$, Debye temperature $\Theta_{\mathrm{D}}$ and Grüneisen constant $\gamma_{\mathrm{G}}$. All quantities are evaluated at the observed equilibrium atomic volume $\Omega_0 = 121.6\,\mathrm{au}$. Phonons are zone-boundary values and experimental data are room-temperature results.

|  | Value | | |
|---|---|---|---|
|  | MGPT | FP LMTO[a] | Experiment |
| **Equation of state** | | | |
| $E_{\mathrm{coh}}$ (eV) | $-8.10^b$ | | $-8.10^c$ |
| $B$ (GPa) | $196^b$ | 192 | $196^d$ |
| $\partial B/\partial P$ | 3.77 | | $3.77^d$ |
| **Vacancy formation** | | | |
| $E_{\mathrm{vac}}^0$ (eV) | $3.20^b$ | 3.27 | |
| **Shear elastic moduli** | | | |
| $C_{44}$ (GPa) | $82.5^b$ | 91.3 | $82.5^d$ |
| $C'$ (GPa) | $52.5^b$ | 55.0 | $52.5^d$ |
| $A = C_{44}/C'$ | 1.57 | 1.67 | 1.57 |
| $\partial C_{44}/\partial P$ | 1.004 | | $1.004^d$ |
| $\partial C'/\partial P$ | 0.984 | | $0.984^d$ |
| **Phase stability** | | | |
| Fcc–bcc (eV) | 0.181 | 0.257 | |
| A15–bcc (eV) | 0.030 | 0.053 | |
| **Phonons** | | | |
| $L[100]$ (THz) | 4.80 | 5.28 | $5.03^e$ |
| $L[110]$ (THz) | 4.88 | 4.52 | $4.35^e$ |
| $T_1[110]$ (THz) | 2.64 | 2.60 | $2.63^e$ |
| $T_2[110]$ (THz) | 2.75 | 4.46 | $4.35^e$ |
| $\Theta_{\mathrm{D}}$ (K) | $226^b$ | | $226^{e,f}$ |
| $\gamma_{\mathrm{G}}$ | 1.69 | | $1.64^d$ |

[a] Söderlind and Moriarty (1998) and Söderlind *et al.* (2000), with the calculated values either interpolated or slightly extrapolated to the volume 121.6 au.

[b] Directly constrained quantity at this volume.

[c] Kittel (1976).

[d] Katahara *et al.* (1979).

[e] Woods (1964).

[f] As calculated from the fitted experimental phonon spectrum.

racy of about 10%, except for the anomalous $T_2[110]$ modes near the zone boundary that occur at low pressures. The corresponding phonon averages such as the Grüneisen constant are nonetheless accurately calculated. The explicit volume dependence of the MGPT potentials also allows for the calculation of accurate stress-dependent bcc dislocation properties over wide ranges of volumes and pressures. The focus in this paper is on ambient conditions, where we have performed a number of additional validation tests on the Ta potentials that are relevant to the dislocation properties considered. These tests will be discussed in detail in §3. In

addition, separate applications of the Ta potentials to high-pressure dislocation properties (Yang *et al.* 2001) and to the high-pressure high-temperature equation of state and melt curve (Moriarty and Söderlind 2001) have also been made.

### 2.3. *Green's function simulation method*

In the present work, the new GF method of Rao *et al.* (1998) for dynamically updating the boundary conditions used in atomistic simulations has been implemented and applied to study the Ta dislocation properties. This approach extends the 2D lattice GF boundary relaxation method originated by Sinclair *et al.* (1979) for treating rigid straight dislocations in 3D simulations, including kink and kink-pair formation. The boundary conditions for 2D and 3D defect simulation cells are evaluated using line (Stroh 1958, 1962) and point (Dederichs and Leibfried 1969) force distributions, respectively. In this flexible-boundary condition method, the simulation cell is divided into three regions, denoted as atomistic, GF and continuum. In the outer continuum region, the atomic positions are initially determined according to the anisotropic elastic displacement field (Stroh 1958, 1962) for a dislocation line defect at the centre of the atomistic region and then are relaxed by GF methods according to the forces in the GF region. Complete atomistic relaxation is performed in the atomistic region according to the interatomic forces generated from equation (1). Forces developed in the GF region as relaxation is achieved in the atomistic region are then used to relax those atoms in *all three* regions by the 2D or 3D elastic and lattice GF solutions for line or point forces. The atomistic and GF relaxations are iterated until all force components on each atom are sufficiently small ($1.0 \times 10^{-4}\,\text{eV}\,\text{Å}^{-1}$ or less), and the final few steps must also be performed by direct atomistic relaxation for the atomistic and GF regions to ensure that there is no force build-up in these two regions.

In our GF simulation code, a spatial domain decomposition scheme is implemented for all three calculational regions, as illustrated schematically in figure 1. The small domain cells defined in this scheme are connected via a cell-linked list method such that each cell has a fixed number of neighbouring cells. This reduces the number of unnecessary interatomic separations considered in evaluating the MPGT potentials, which is crucial to their efficient application. A detailed description of the technique will be published elsewhere (Yang and Moriarty 2001), and here we only elaborate a few additional key features of our approach. In general, there are three central issues that need to be addressed:

(1) the geometry of the simulation cell, which is purely cylindrical for a straight dislocation and in the form of a series of displaced cylindrical discs for a kink;

(2) the fact that there are three regions in the full simulation cell, so that a connectivity algorithm for information passing between different regions is therefore necessary;

(3) the large effective cut-off radius $R_{\text{cut}} = 4.25 R_{\text{WS}} (\approx 2 R_0)$ for the MGPT potentials, which means that there is a large overhead associated with the number of atoms per cell if the conventional domain-cell partition is considered (i.e. if each cell covers a volume $R_{\text{cut}}^3$ which here contains about 16 atoms).

To solve these problems, a so-called layered-cake decomposition is used to split the three regions in the full simulation cell, so that each region has its own domain
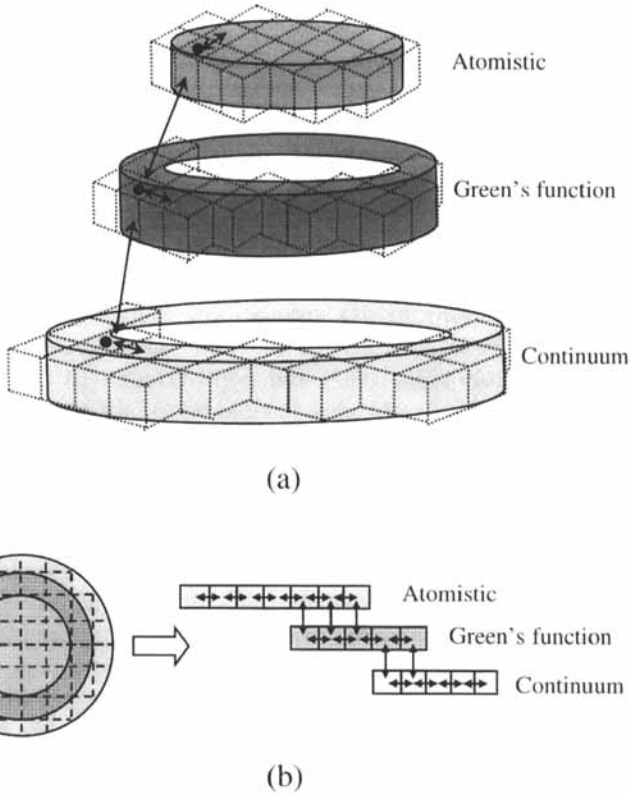
(a)



(b)

Figure 1.   Schematic representations of the domain decomposition scheme used to implement GF-based flexible-boundary conditions in our MGPT simulation code for the present dislocation calculations. (*a*) The three main computational regions separated into a layered-cake structure for a cylindrical coordinate system such that each region has its own domain decomposition. (*b*) To ensure the connectivity between regions and compatibility with parallel computing platforms, the domain cells are mapped into three one-dimensional arrays (1D) with cell-linked pointers between the cells and overlap regions.

cell-linked list. To reduce the overhead associated with the number of atoms per cell, the cell sizes are reduced by a factor of eight; therefore the average number of atoms per cell is about two. In addition, this approach allows a better description of the cylindrical geometry involved in the simulation when a cubic domain decomposition is used. We have found the performance of our GF MGPT simulation code has thereby been increased by an order of magnitude compared with conventional domain decomposition methods.

To take advantage of the scalable architectures of the current state-of-the-art computer platforms, a mapping algorithm has also been developed for massively parallel computers. A 3D to 1D mapping list is built at the beginning of the simulation. This mapping list ensures the connectivity between different regions, so that no information is lost during the simulation. The logic behind the present algorithm is that our simulation is always performed in a 1D computer simulation domain regardless of the physical geometry involved. This is particularly useful when dealing with complicated geometries such as kinked dislocation structures and dislocation–dislocation interactions.

## §3. VALIDATION TESTS OF MODEL GENERALIZED PSEUDOPOTENTIAL THEORY POTENTIALS

The present Ta potentials have been rather extensively validated for a wide variety of deformation and defect properties at both ambient pressure and high pressures, using available experimental data as well the results of *ab-initio* electronic structure calculations. Here, we consider several properties that are expected to have a significant influence on bcc mechanical behaviour and for which experimental and/ or *ab-initio* data exist near ambient conditions. These properties are the ideal shear strength, *relaxed* vacancy and self-interstitial formation and migration energies, grain-boundary atomic structure and the generalized stacking-fault energy ($\gamma$) surfaces for the {110} and {211} slip planes. The $\gamma$ surface validation is particularly important in the present context because of the close association of these surfaces with the screw dislocation properties (Duesbery and Vitek 1998).

### 3.1. *Ideal shear strength*

We first consider the ideal theoretical shear strength, as defined for a bcc metal by Paxton *et al.* (1991). These workers identified the shear strength of the perfect crystal with the maximum stress $\tau_c$ required for a continuous homogeneous deformation of the crystal into itself via the observed twinning mode. For bcc metals, this mode can be specified by a shear direction $\boldsymbol{\eta} = [\bar{1}\bar{1}1]$ and a normal plane $\mathbf{K} = (112)$. In the absence of tensile relaxation normal to $\mathbf{K}$, which has been shown to be small for bcc transition metals (Paxton *et al.* 1991, Morris *et al.* 2000), the atomic positions during the deformation can be very simply related to the relative amount of shear $x/s$ along the twinning path. In particular, the unrelaxed calculation may be carried out entirely using a single atom per unit cell and periodic boundary conditions, allowing for direct application of the FP LMTO electronic structure method. Previously for Ta, full self-consistent FP LMTO calculations of the unrelaxed ideal shear strength were performed at five selected volumes in the 0–1000 GPa pressure range (Söderlind and Moriarty 1998). Those calculations have been repeated here at the observed equilibrium volume $\Omega_0$ to compare with MGPT Ta calculations performed under the same conditions.

With either the FP LMTO or the MGPT method, we calculate a symmetric energy barrier along the twinning path:

$$W(x) = \frac{E_{\text{tot}}[x] - E_{\text{tot}}[0]}{N}, \tag{7}$$

with a barrier height $W_c$ at $x = s/2$. The corresponding stress along this path is given by

$$\tau(x) = \frac{1}{\Omega_0}\frac{\mathrm{d}W(x)}{\mathrm{d}x}. \tag{8}$$

The ideal shear strength is then identified with the maximum calculated stress along the twinning path, $\tau_c = \tau(x_c)$, where $x_c$ is the critical shear separating regimes of elastic and plastic deformation of the crystal. In the FP LMTO case, $W(x)$ has been calculated at a total of 11 points in the range $0 \leqslant x \leqslant s/2$ and extended to $x = s$ by symmetry. The result has then been numerically differentiated to obtain $\tau(x)$ via equation (8). The latter displays a small amount of numerical noise but may be adequately fitted with a smooth polynomial. In the MGPT case, $W(x)$ has been calculated at small intervals of 0.01 over the full range $0 \leqslant x \leqslant s$, and then a smooth

$\tau(x)$ curve has been obtained directly from numerical differentiation. The FP LMTO and MGPT results are plotted and compared in figure 2. Calculated values of the barrier height $W_c$, critical stress $\tau_c$, relative critical shear $x_c/s$ and corresponding shear modulus in the $\langle 111 \rangle$ direction given by

$$G = \frac{2C' + C_{44}}{3}, \tag{9}$$

are listed and compared in table 2. The overall agreement of the FP LMTO and MGPT results is quite reasonable, although the MGPT values of $W_c$ and $\tau_c$ are about 14% and 23% larger than the FP LMTO values respectively. This level of agreement is similar to that found previously for Mo (Xu and Moriarty 1996).

### 3.2. *Point-defect formation and migration*

Next we consider relaxed point-defect calculations of the single isolated vacancy and self-interstitial in bcc Ta. These defects are modelled within a large computa-
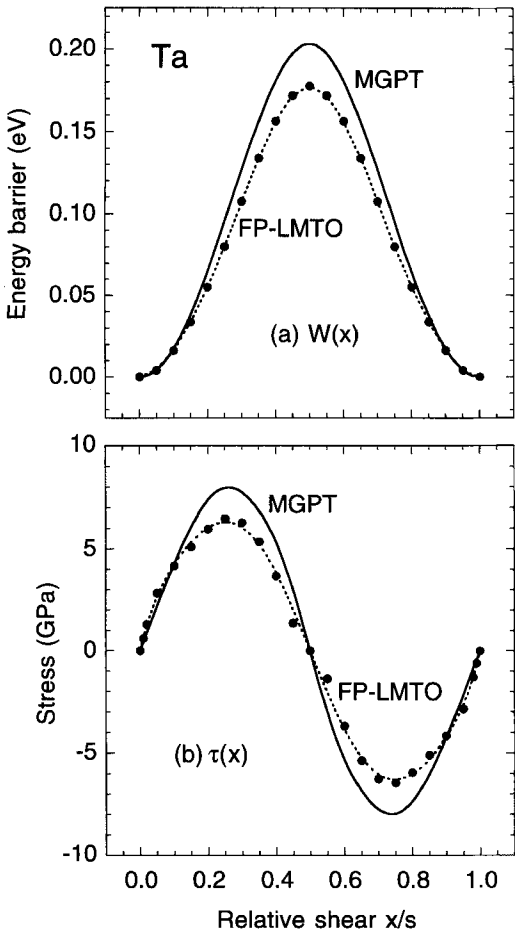


Figure 2.   Unrelaxed ideal shear strength in bcc Ta, as calculated with the *ab-initio* FP LMTO electronic structure method and with the present MGPT interatomic potentials: (*a*) energy barrier $W(x)$ along the prescribed $(112)$–$[\bar{1}\bar{1}1]$ twinning path; (*b*) corresponding shear stress $\tau(x)$ along the same path.

Table 2.   Ideal theoretical shear strength of bcc Ta, without tensile relaxation: barrier height $W_c$, relative critical shear $x_c/s$, critical stress $\tau_c$ and shear modulus $G$. All quantities are evaluated at the observed equilibrium atomic volume $\Omega_0 = 121.6$ au.

|        | $W_c$ (eV) | $x_c/s$ | $\tau_c$ (GPa) | $G$ (GPa) | $\tau_c/G$ |
|--------|------|------|------|------|------|
| MGPT   | 0.20 | 0.26 | 8.0  | 62.5 | 0.13 |
| FP LMTO | 0.18 | 0.26 | 6.5  | $67.1^a$ | 0.10 |

$^a$ Söderlind and Moriarty (1998), with the calculated value slightly extrapolated to the volume 121.6 au.

tional supercell containing $N$ atoms in a volume $\Omega_N$, with periodic boundary conditions applied in all three directions. The formation energy for the defect is defined as

$$E^f = E_{tot}[N, \Omega_N] - NE_{coh}, \qquad (10)$$

where $E_{tot}$ is the total energy of the simulated system including the defect and $E_{coh}$ is the cohesive energy per atom of the bulk solid at the equilibrium atomic volume $\Omega_0$. The corresponding formation volume is

$$\Omega^f = \Omega_N - N\Omega_0. \qquad (11)$$

Equations (10) and (11) can be applied with the PP and FP LMTO electronic structure methods as well as with the MGPT potentials and are intended to include both volume and structural relaxation. Inclusion of volume relaxation necessitates that $\Omega_0$ in these equations be interpreted as the calculated zero-temperature equilibrium volume. With the PP and FP LMTO methods, a 54-atom supercell is normally used here in the vacancy calculations, corresponding to $N = 53$, and this provides ample convergence (Söderlind *et al.* 2000). For the corresponding PP self-interstitial calculations, a 48-atom supercell has been used, corresponding to $N = 49$. Only the $\langle 110 \rangle$ split-dumbbell configuration of the self-interstitial has been considered, which has previously been shown to be the lowest-energy configuration for Mo (Xu and Moriarty 1996).

With the MGPT method, supercell size is not an important limitation; so much larger cells have been used to ensure convergence, corresponding to $N = 249$ for the vacancy and $N = 1801$ for the self-interstitial. In addition, there is a useful alternative approach that has also been used with the MGPT potentials and avoids the volume relaxation calculation. In this approach, one works with a cell of fixed volume $\Omega_N = (N \pm 1)\Omega_0$ and calculates the formation energy at constant atomic volume $\Omega_0$ according to

$$E^f = E_{tot}[N, (N \bullet 1)\Omega_0] - NE_{coh} \pm \Omega_0 P_{vir}, \qquad (12)$$

where the upper sign is for a vacancy and the lower sign is for a self-interstitial. The quantity $P_{vir}$ is the so-called virial pressure as given by Moriarty (1990b) that is needed to maintain constant atomic volume. Under these conditions, the formation volume may be calculated by the expression (Harder and Bacon 1986)

$$\Omega^{f} = -\frac{\Omega_0}{B}\frac{dE^f}{d\Omega}, \tag{13}$$

where $B$ is the bulk modulus.

To calculate the corresponding migration energy barrier, we move one atom, which is either the interstitial atom or a nearest-neighbour atom in the vacancy case, from its equilibrium site towards a nearest-neighbour site or the vacancy site respectively. During the migration process, the migrating atom is allowed to relax in the plane perpendicular to the migration path. At the same time, all other atoms are fully relaxed according to the forces acting on them minus the average force component along the migration direction due to the migrating atom. In this way, one prevents a rigid shift of the simulation cell while allowing location of the correct saddle point along the path. The migration energy is then given by

$$E^{m} = E^{\text{saddle}} - E^{f}, \tag{14}$$

where $E^{\text{saddle}}$ is the formation energy of the defect at the saddle point calculated using either equation (10) or equation (12). Here the assumed migration paths are taken along $\langle 111 \rangle$ for both the vacancy and the self-interstitial, with the latter corresponding to the so-called jump and rotation path, previously calculated to be the one of lowest energy for Mo with both MGPT (Xu and Moriarty 1996) and FS (Harder and Bacon 1986) potentials.

Table 3 displays our calculated vacancy and self-interstitial formation and migration energies and formation volumes for Ta using the FP LMTO, PP and MGPT methods, together with available experimental data. Clearly, there is good agreement between theory and experiment, between the electronic structure results and the MGPT results, and between the use of equations (10) and (11) and equations (12) and (13). In particular, note that the characteristic low vacancy migration energy of group-V metals such as Ta is well calculated by the MGPT potentials.

Table 3. Vacancy and $\langle 110 \rangle$ split-dumbbell self-interstitial formation energies $E_{\text{vac}}^{f}$ and $E_{\text{int}}^{f}$, migration energies $E_{\text{vac}}^{m}$ and $E_{\text{int}}^{m}$, and formation volumes $\Omega_{\text{vac}}^{f}$ and $\Omega_{\text{int}}^{f}$ for bcc Ta. The PP and FP LMTO vacancy results were obtained from fully relaxed 54-atom supercell calculations, using ten special $k$ points, except as noted. The PP self-interstitial results were obtained from corresponding 48-atom supercell calculations. Migration energies were calculated along $\langle 111 \rangle$ migration paths, as described in the text.

| | $E_{\text{vac}}^{f}$ (eV) | $E_{\text{vac}}^{m}$ (eV) | $\Omega_{\text{vac}}^{f}/\Omega_0$ | $E_{\text{int}}^{f}$ (eV) | $E_{\text{int}}^{m}$ (eV) | $\Omega_{\text{int}}^{f}/\Omega_0$ |
|---|---|---|---|---|---|---|
| MGPT[a] | 2.89 | 0.78 | 0.53 | 6.30 | 0.50 | |
| MGPT[b] | 3.08 | | 0.51 | 6.37 | | 0.4 |
| PP[b] | 3.10 | 0.90 | 0.60 | 6.65 | 0.60 | 0.2 |
| FP LMTO[b] | 3.10 | 0.74[c] | | | | |
| Experiment[d] | 2.8–3.1 | 0.7 | | | | |

[a] Via equations (12) and (13) at atomic volume $\Omega_0 = 121.6$ au, with full structural relaxation.
[b] Via equations (10) and (11), with both volume and structural relaxation.
[c] 36-atom supercell calculation.
[d] Schultz and Ehrhart (1991).

Table 4. Atomic structure of the $\Sigma = 5$, (310)–[001] grain boundary in bcc transition metals, as predicted from MGPT interatomic potentials and as measured in HREM experiments. $a_0$ is the bulk lattice constant.

| Metal | Mirror Symmetry | | [001] displacement (units of $a_0$) | |
|---|---|---|---|---|
| | MGPT | HREM | MGPT | HREM |
| Nb[a] | Yes | Yes | 0.0 | 0.0 |
| Mo[b] | No | No | 0.2 | $0.25 \pm 0.05$ |
| Ta[c] | No | No | 0.17 | $0.17 \pm 0.05$ |

[a] Campbell *et al.* (1993).
[b] Campbell *et al.* (1999).
[c] Campbell *et al.* (2000).

### 3.3. *Grain-boundary atomic structure*

The prediction of grain-boundary atomic structure represents an important validation test for interatomic potentials because this is the one example of an extended defect where direct comparison with experiment is possible. Here we very briefly mention recent MGPT simulations and experimental measurements on the $\Sigma = 5$, (310)–[001] symmetric tilt boundary in prototype bcc transition metals, including Ta (Campbell *et al.*, 1993, 1999, 2000). This particular boundary is of special interest for several reasons. First, it has been possible to fabricate high-quality bicrystals for this orientation and to study them experimentally with high-resolution transmission electron microscopy (HREM). Second, it turns out that the distributions of bond lengths and bond angles at this boundary are similar to those occurring in the vicinity of a bulk screw dislocation; so relevant aspects of the MGPT potentials are indeed being tested. Finally, the actual atomic structure of the grain boundary is not a generic feature of bcc metals but rather is material dependent and is a sensitive test of the angular forces (Campbell *et al.* 1993, Ochs *et al.* 2000).

The two main structural issues for the $\Sigma = 5$, (310)–[001] grain boundary are whether or not mirror symmetry is preserved across the boundary and, if not, what the magnitude of the relative atomic displacement along the [001] tilt axis is. Calculated MGPT and measured HREM results for Nb, Mo and Ta are summarized and compared in table 4. In each case, the symmetry of the grain boundary has been correctly predicted by the MGPT potentials. In Mo and Ta, where the mirror symmetry is broken, the [001] atomic displacement is also quantitatively consistent with experiment. Further details for the case of Ta have been discussed by Campbell *et al.* (2000).

### 3.4. *Generalized stacking-fault energy* ($\gamma$) *surfaces*

For accurately modelling bcc screw dislocation behaviour, perhaps the most important validation test concerns the generalized stacking-fault energy or $\gamma$ surfaces, as defined by Vitek (1974). The $\gamma$ surface is an energy profile of two semi-infinite blocks of bulk crystal rigidly displaced relative to each other by a vector **u** in a chosen fault plane, with atomic relaxation allowed only perpendicular to the plane. The $\gamma$-surface energies can be calculated using an appropriate computational super-cell with periodic boundary conditions. Most often, this has been done using two fault surfaces per supercell, so that the full translational symmetry of the bulk crystal

is preserved. Alternatively, one can use one fault surface per supercell if one of the lattice vectors defining the cell is inclined along the displacement direction **u**. In this way, the number of atoms needed to define the supercell is reduced by half, making *ab-initio* electronic structure calculations of high-symmetry features of the $\gamma$ surface much more tractable. We follow the latter approach and use a supercell consisting of at least 12 atomic planes perpendicular to the fault surface and with one half of the cell shifted by the displacement vector $\mathbf{u} = \alpha \mathbf{u}_{max}$, where $0 \leqslant \alpha \leqslant 1.0$. The same approach can then be applied to MGPT, FP LMTO or PP calculations.

Complete $\{211\}$ and $\{110\}$ $\gamma$ surfaces have been calculated for bcc Ta with the present MGPT potentials. These results are displayed in figure 3. Supercell size is not a limitation in these calculations, and larger cells consisting of 48 atomic planes (48 atoms) for the $\{211\}$ surface and 16 planes (32 atoms) for the $\{110\}$ surface have been used to ensure full convergence. Qualitatively, the calculated surfaces display the well known general features expected for bcc metals (Vitek 1974). The $\{110\}$ surface is fully symmetric, while the $\{211\}$ surface reveals the twinning–antitwinning asymmetry characteristic of bcc materials. No stable stacking faults in the form of local minima are found on either surface, and all extrema are either maxima or saddle points. The specific issue that we wish to address here is the quantitative accuracy of these surfaces.
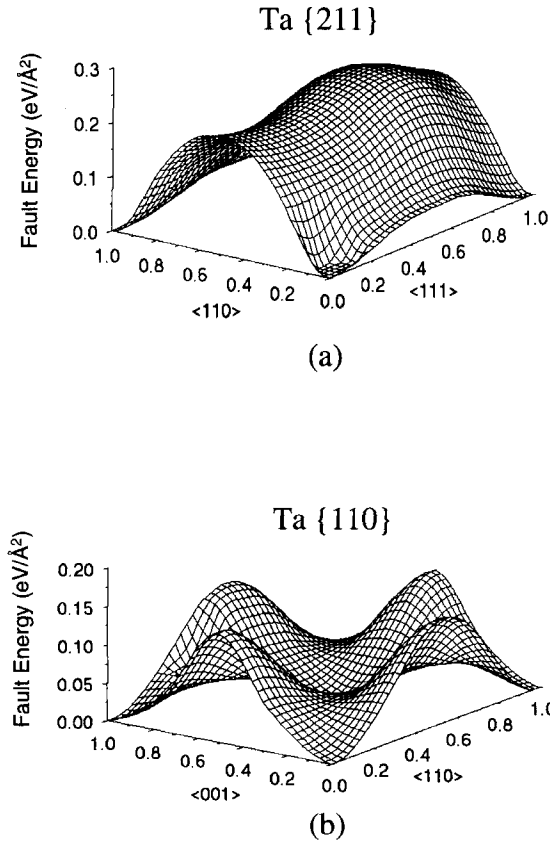


Figure 3.   Calculated generalized stacking-fault or $\gamma$ energy surfaces for bcc Ta from the present MGPT interatomic potentials: (*a*) $\{211\}$ surface; (*b*) $\{110\}$ surface.
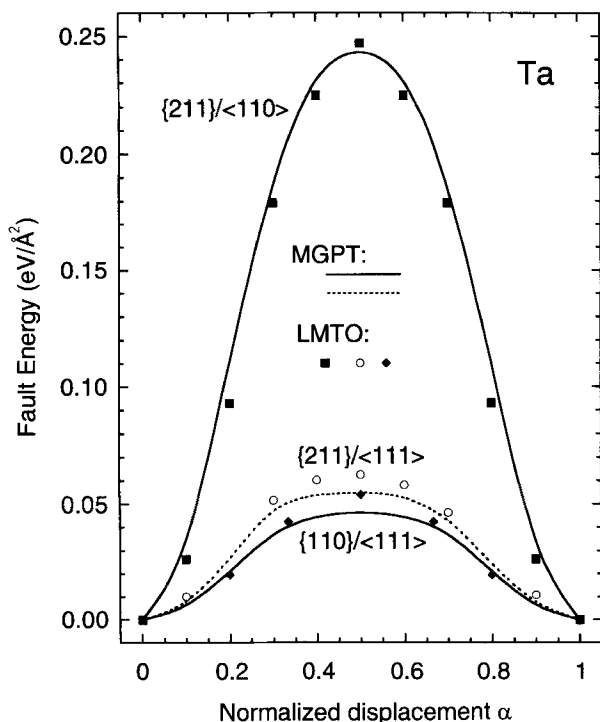
Figure 4. High-symmetry lines in the {211} and {110} $\gamma$ surfaces for bcc Ta, as calculated with the *ab-initio* FP LMTO electronic structure method and with the present MGPT interatomic potentials.

In order to validate the MGPT potentials in this context, we have studied high-symmetry slices of the {211} and {110} surfaces using the FP LMTO method. The specific geometries considered were two slices of the {211} surface defined by the displacement vectors along $\langle 111 \rangle$ and $\langle 110 \rangle$ and one slice of the {110} surface along $\langle 111 \rangle$. We first generated relaxed atomic configurations for these geometries by performing 12-plane *ab-initio* PP supercell calculations. We then applied these same configurations to both FP LMTO and MGPT calculations of $\gamma$-surface energies for the defined geometries. The results so obtained are compared in figure 4. The agreement is generally very good and quantitatively the MGPT energies agree with the FP LMTO results everywhere to within 15%. In particular, the calculations along $\langle 111 \rangle$ provide a very sensitive test of the quality of the MGPT potentials because the stacking-fault energies involved are very small. We conclude that the MGPT is reasonably accurate for the calculation of the $\gamma$ surfaces of Ta, and this in turn gives us confidence that the MGPT will also perform well for the $(a/2)\langle 111 \rangle$ screw dislocations.

§4. $(a/2)\langle 111 \rangle$ SCREW DISLOCATION PROPERTIES

In bcc metals, the mobility of an $(a/2)\langle 111 \rangle$ screw dislocation is severely restricted by the atomic structure of its core. The origin of this particular feature was first explained by Hirsch (1960) using a symmetry argument. Around a given $\langle 111 \rangle$ direction, the bcc structure has threefold symmetry. Each $\langle 111 \rangle$ direction also

contains three {110} and three {112} planes which are potential core dissociation and slip planes in the bcc structure. These properties lead to the possibility of a 3D spreading of the core structure when the screw dislocation is formed. Descriptions of such an extended core in terms of directional splitting have resulted from many previous studies (Duesbery *et al.* 1973, Vitek 1974, Duesbery 1984a, b, Xu and Moriarty 1996, 1998, Duesbery and Vitek 1998). Such studies have indicated a core extension of a few Burgers vectors and a high Peierls stress associated with its movement, so that only atomistic methods are able to capture the details and to explain the mobility of the screw dislocations in bcc metals. In this section, we discuss our atomistic simulations on basic $(a/2)\langle 111 \rangle$ screw dislocation core properties in bcc Ta using our new MGPT potentials and GF methodology. Our focus will be on the zero-temperature calculation of core properties that are fundamental to an understanding of dislocation structure and mobility. The properties considered are the atomic structure and energy of the unstressed dislocation core, the nature and energetics of isolated kinks and mobile kink pairs that can he formed from this core in the low-stress limit, and the orientation dependence of the Peierls stress required to move the rigid dislocation in the high-stress limit.

### 4.1. *Core structure and energy*

The $(a/2)\langle 111 \rangle$ screw dislocation has one or more stable core configurations located at the centre of gravity of three $\langle 111 \rangle$ atomic rows forming a triangle. Around these three rows the near-neighbour atoms are located on a helix that winds up in a clockwise or counterclockwise manner, depending on the location of the elastic centre and the sign of the Burgers vector, so that two different types of core configuration can be obtained (Xu and Moriarty 1996). One configuration is isotropic and of high energy and may or may not be stable. This is often referred to as the 'hard' core. The other configuration is of low energy and is normally the stable ground-state structure. This is the so-called 'easy' core. In general, the 'easy' core exhibits threefold directional spreading and is doubly degenerate, but under some circumstances this spreading may become isotropic and a non-degenerate core with a higher sixfold symmetry results. In the present work, we have studied only the 'easy'-core ground state of bcc Ta.

The stable ground-state screw dislocation core structure in Ta has been simulated using the 2D GF technique in cylindrical geometry, with periodic boundary conditions and a period of $b = 3^{1/2}a/2$ along the $z$ axis ($\langle 111 \rangle$ direction), where $b$ is the magnitude of the Burgers vector (2.86 Å) and $a$ is the bcc lattice constant (3.30 Å). An infinite $(a/2)\langle 111 \rangle$ screw dislocation was first introduced by displacing all atoms in the simulation according to anisotropic elasticity solutions using Stroh's (1958, 1962) sextic formalism. Radially outwards from the cylinder axis, the inner atomistic region of the simulation cell was surrounded by GF and continuum regions each with a shell thickness of $R_{\text{cut}} = 4.25R_{\text{WS}}$, the effective cut-off radius for the MGPT potentials. The optimum radius for the atomistic region was found to be about $20b$. This rather large value was necessary here to distinguish accurately between the threefold and sixfold symmetric core and to ensure that there were no size effects present in our final results. The final relaxed atomic core positions were determined by alternatively freezing the continuum and GF regions, while allowing the atomistic region to come to equilibrium by use of truncated quasi-Newton and GF relaxation procedures. In order to ensure the absolute minimum-energy structure, the initial elastic centre of the core was varied inside the triangle formed by three central atomic

rows. As expected, the stable configuration was found with the elastic centre located at the centre of gravity of the central triangle.

A nearly isotropic but still threefold symmetric and doubly degenerate core structure is predicted for Ta. The core structure is most readily quantified by its so-called polarization. The two energetically equivalent configurations of the degenerate core display a broken symmetry arising from a simultaneous translation, parallel to the dislocation line but in the opposite sense for the two different core orientations, of the three central atoms nearest to the core centre. This property was first realized by Duesbery *et al.* (1973) and later was termed the polarity (or polarization) of the dislocation core by Seeger and Wüthrich (1976). By symmetry, the polarization vector $\mathbf{p}$ can only vary uniquely from $-\mathbf{b}/6$ to $\mathbf{b}/6$. At $\mathbf{p} = 0$, the two core configurations coincide and a fully symmetric or isotropic core structure with a higher sixfold symmetry is obtained. At $\mathbf{p} = \pm\mathbf{b}/6 = \pm0.167\mathbf{b}$, on the other hand, a fully polarized core is obtained with maximum threefold spread out along $\langle 112 \rangle$ directions. For Ta near ambient pressure and the present assumed conditions (hydrostatic pressure $P = -1$ GPa corresponding to the observed 300 K equilibrium volume), the two core configurations are found to have a very small polarization magnitude $p = 0.004(b/6)$, resulting in a nearly isotropic core structure.

The full equilibrium configuration calculated for the Ta $(a/2)\langle 111 \rangle$ screw dislocation core is most easily displayed using the standard differential displacement (DD) method (Vitek 1974). In the DD method, the $\langle 111 \rangle$ screw components of the relative displacement of neighbouring atoms due to the dislocation (i.e. the total relative displacement in the $z$ direction less than that in the perfect lattice) is represented by an arrow between the two atoms. The calculated screw-component DD map for Ta is shown in figure 5 (*a*). A corresponding map can also be constructed for the edge components of the dislocation as well. For the edge displacements, the direction of the arrow indicates the direction of the relative displacement component normal to the $\langle 111 \rangle$ Burgers vector. The calculated edge-component DD map is displayed in figure 5 (*b*). For the screw components, the length of the arrows is normalized by $(a/6)\langle 111 \rangle$, the magnitude of the separation of neighbouring atoms. For the edge components, the arrows have been magnified by a factor of ten to make them clearly visible in the figure.

Our calculated core structure for Ta may also be compared with other recent calculations by different methods. Duesbery and Vitek (1998) obtained an isotropic sixfold symmetric core using FS potentials in a fixed-boundary-condition atomistic simulation. An isotropic core structure for Ta was also obtained by Ismail-Beigi and Arias (2000) in the first *ab-initio* PP dislocation calculation. In the latter calculation a quadrupolar arrangement of four dislocation cores in a small computational cell containing only 90 atoms with periodic boundary conditions was considered. While the differences between the three approaches is clearly substantial, it is interesting that all three conclude that the equilibrium Ta core structure is either isotropic or nearly so. Our studies reveal the additional interesting result that the precise core structure depends sensitively on the volume or pressure conditions considered. We find that the core polarization is, in fact, a rather rapidly increasing function of pressure, as illustrated in figure 6 up to 20 GPa. At higher pressures, this effect is even more dramatic and large polarizations can occur (Yang *et al.* 2001). Conversely, under modest expansion (i.e. negative pressure), the polarization will indeed exactly vanish. Thus in general, one can expect a continuum of $(a/2)\langle 111 \rangle$ screw dislocation core structures between the isotropic and fully polarized limits.
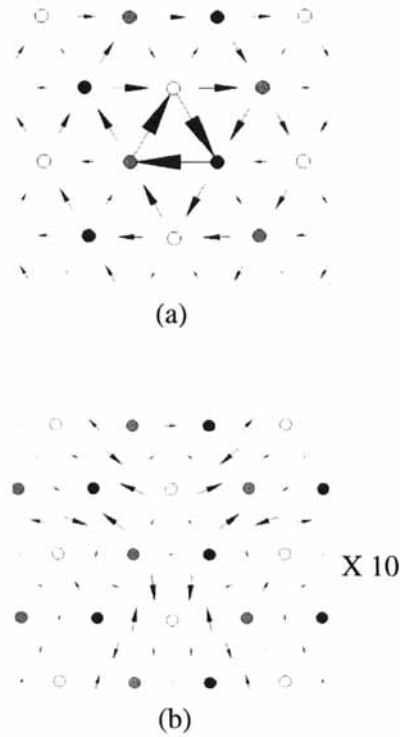
(a)

(b)

X 10

Figure 5.  The core structure of the $(a/2)\langle 111 \rangle$ screw dislocation in bcc Ta, as obtained with the present MGPT potentials: (*a*) differential displacement map of the screw components of the core; (*b*) corresponding map of the edge components, magnified by a factor of ten.
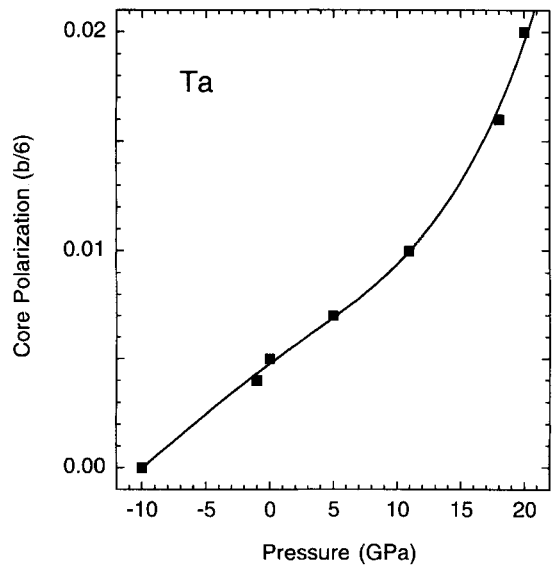


Figure 6.  Pressure dependence of the core polarization in bcc Ta, as calculated from the present MGPT interatomic potentials (■): (———), polynomial fit to the calculated points.

In addition to its atomic structure, we have also calculated the effective size and energy associated with the core, as follows. In continuum elasticity theory, the formation energy $E^f$ of a dislocation in a cubic crystal is a linear function of $\ln(R/R_c)$, where $R$ is the outer radius of a cylinder which contains the dislocation core at its centre and $R_c$ is the core radius. The formation energy includes the core energy $E^f_{core}$ stored inside $R_c$, plus the elastic energy stored in the region between $R_c$ and $R$, such that

$$E^f = E^f_{core} + A \ln\left(\frac{R}{R_c}\right), \tag{15}$$

where the elastic coefficient $A$ can be directly related to the bulk elastic moduli of the material (Xu and Moriarty 1996). To determine the core size and energy, we have first estimated $R_c$ by comparing the 2D elastic and lattice GFs as a function of $R$. Specifically, we find $R = R_c = 1.75b$ to be the radius at which the elastic and lattice GF components $G_{33}$ become identical, as shown in figure 7 (*a*). To compare with
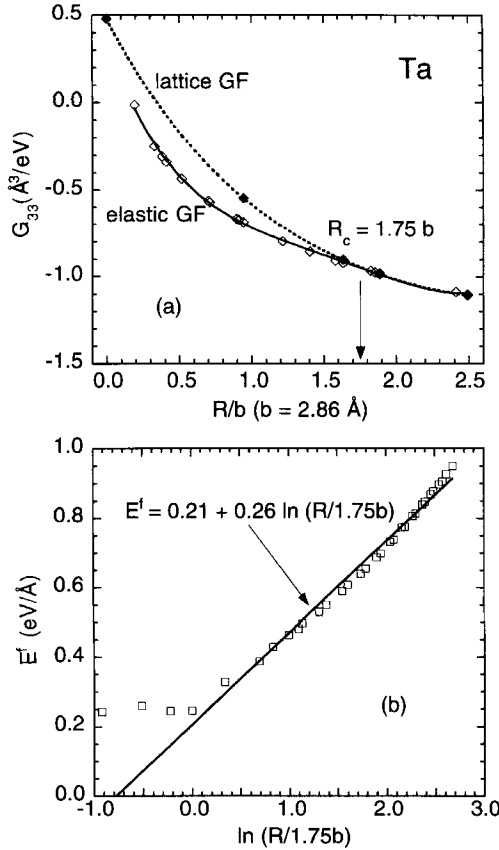
Figure 7. (*a*) The elastic and lattice GF component $G_{33}$ as a function of distance $R$ from the dislocation centre for bcc Ta. The point where these curves join is identified with the core radius $R_c = 1.75b$. (*b*) The $(a/2)\langle 111 \rangle$ screw dislocation formation energy as a function of $\ln(R/1.75b)$, as simulated with the present MGPT potentials (■) and fit to the analytic form of equation (15) (——).

equation (15), the dislocation formation energy has then been calculated from ato-
mistic simulations, using equation (10) and varying the size of cylindrical radius $R$
from 4 to 60 Å. Plotting the formation energy $E^{\mathrm{f}}$ as a function of $\ln{(R/1.75b)}$, we
find that the calculated data fall reasonably well on to a straight line for $R > 1.75b$,
as shown in figure 7(*b*). We have thereby determined $E^{\mathrm{f}}_{\mathrm{core}} = 0.21\,\mathrm{eV\,\mathring{A}^{-1}}$ and
$A = 0.26\,\mathrm{eV\,\mathring{A}^{-1}}$. The latter is very close to the value of $A = 0.27\,\mathrm{eV\,\mathring{A}^{-1}}$ that one
calculates directly from the elastic moduli.

### 4.2. *Isolated kinks and kink-pair formation*

At finite temperatures, the motion of the screw dislocations in the bcc lattice
normally occurs by the thermally assisted formation and migration of kink pairs.
For low-stress conditions, the individual kinks in a kink pair are well separated and
weakly interacting; so kink-pair formation can be studied by just looking at isolated
kink formation. In this limit, the nature and atomic structure of the possible kinks
are closely related to the unstressed dislocation core. As we have indicated above, the
doubly degenerate stable core structure of the rigid $(a/2)\langle 111\rangle$ screw dislocation in
Ta can have two energetically equivalent configurations with opposite polarizations,
commonly denoted as positive p and negative n. As a result, there are different
possible kinks and kink-pair configurations involving p and n segments that can
be formed. In addition, p and n segments can coexist on the same dislocation line
in the form of a so-called antiphase defect (APD). This further increases the multi-
plicity of possible kinks and kink pairs.

The 3D simulation of an isolated kink in bcc Ta is divided into three general
steps. In the first step, the two symmetry-related core segments (say, p and n) of the
screw dislocation that will make up the arms of the kink are constructed in neigh-
bouring equilibrium sites separated by the intended kink height $h$. Next, these con-
figurations are used together with the 3D GF technique to set up the initial
conditions for the full kink simulation. To avoid a sharp transition from one arm
of the kink to the other arm, the initial configuration contains a transition region of
length $11b$ located in the middle of the simulation cell. The atomic positions in the
transition region are obtained by placing the elastic centres in the plane containing
the two kink arms, with positions changing from 0 to $h$ in increments $0.1h$. The
simulation geometry is indicated schematically in figure 8. Finally, a combination
of conjugate-gradient (i.e. molecular statics) and 3D GF techniques are used to relax
the system fully and to obtain the structure and formation energy of an isolated kink
with very small residual forces ($10^{-4}\,\mathrm{eV\,\mathring{A}^{-1}}$ or less) left in the atomistic and GF
regions of the simulation cell.

To model an isolated kink accurately, the simulation cell is taken in the form of a
long compliant cylinder (made up of unit discs) of radius $20b$ (for the atomistic
region) and a total length $(60–80)b$ centred on the dislocation line. To form a 3D
cage, the two ends of the cylinder are capped with GF and continuum regions. The
maximum needed length of the simulation cell can be roughly estimated from a
simple continuum expression for the kink width, $\omega_{\mathrm{kink}} = (\pi h b G/\tau_{\mathrm{P}})^{1/2}$, where $G$ is
the shear modulus and $\tau_{\mathrm{P}}$ is the Peierls stress (Patukhov 1983). Using a value of
$\tau_{\mathrm{P}} \approx 10^{-2}G$, $\omega_{\mathrm{kink}} \approx 17b$ for an elementary kink on a $\{110\}$ plane. We take the total
simulation cell length to be about $5\omega_{\mathrm{kink}}$ to ensure a smooth transition region for the
kink formation. In practice, our calculated kink widths are actually smaller than $17b$,
so that shorter cell lengths than $80b$ are usually possible. The $z$ axis is of the com-
pliant cylinder is taken parallel to the [111] dislocation line direction, while the $y$ axis
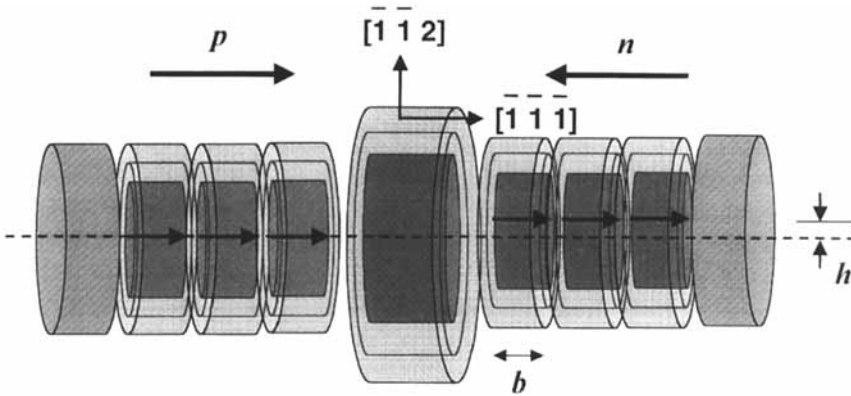
Figure 8. Schematic representation of the present 3D atomistic modelling geometry for an isolated pln dislocation kink. The arms of the king are represented by a series of unit cylindrical discs, each with atomistic, GF and continuum simulation regions. The large transition region between the arms (actually $11b$ in length) represents a series of 11 discs initially displaced along $[\bar{1}\bar{1}2]$ by $0.1h$, where $h$ is the kink height. The fundamental kink is formed on the (110) plane with kink height $h = 6^{1/2}a/3$.

is taken parallel to $[1\bar{1}0]$ and the $x$ axis to $[\bar{1}\bar{1}2]$. The smallest repeat translation vector for the rigid screw dislocation core in the bcc lattice is $(a/3)[\bar{1}\bar{1}2]$ on a (110) plane, and this defines the elementary kink height $h$ with magnitude $6^{1/2}a/3$. We consider here only kinks formed within this geometry. Kinks formed on other planes such as {211} have significantly larger kink heights and therefore are either unstable or have much larger kink formation energies (Xu and Moriarty 1998; M. S. Duesbery 1999, unpublished).

Because of the two equivalent configurations of the degenerate core, two different APDs on the dislocation line (np and pn) and six distinct and non-degenerate kinks arc geometrically possible (Duesbery 1983a, b). The latter depend on whether the kink in question forms the left- or right-hand member (denoted by $l$ or $r$ respectively) of a kink pair, and on which core configuration (n or p) is assumed by the adjacent dislocation arms. The kinks nln and plp are degenerate, as are nrn and prp. The remaining four non-degenerate kinks are nlp, pln, nrp and prn. The formation energies of the APDs and isolated kinks have been calculated with the simulation cell partitioned into cylindrical discs, each aligned parallel to the dislocation line and of thickness one Burgers vector. The formation energy of the defect (APD or kink) is then given by summing the atom to atom energy difference between discs in the defect configuration and exactly similar discs in a reference configuration containing only the rigid screw dislocation. The complete spectrum of formation energies of possible isolated APDs and kinks are listed in table 5. In situations where the left- or right-hand nature of the kink is otherwise identified, as in the present tables, a short-hand notation is used in which, for example, nln is replaced by simply nn to denote a specific kink. The disc-by-disc energy profile of a kink also gives a clear measure of its width and the distribution of the formation energy within the kink. A typical profile for the pln kink in Ta is plotted in figure 9. From this result we infer that kink half-width is about $3.4b$, so that $\omega_{kink} \approx 7b$.

At large separations, a general kink pair can be formed from any pair of isolated left and right single kinks taken from table 5, with the addition of one or more

L. H. Yang *et al.*

Table 5.  APD and isolated kink formation energies for
         $(a/2)\langle 111\rangle$ screw dislocations in bcc Ta, as calcu-
         lated with the present MGPT potentials.

| | Formation energy (eV) | | |
| Configuration | APD | Left kink | Right kink |
|---|---|---|---|
| nn |      | 0.61 | 0.43 |
| pp |      | 0.61 | 0.43 |
| np | 0.23 | 0.69 | 0.54 |
| pn | 0.03 | 0.42 | 0.63 |

APDs, as necessary, to maintain the continuity of the dislocation core polarization. With zero, one or two APDs, there are a total of 16 kink pairs that can be formed. These are elaborated in table 6. The formation energy $E_{kp}^f$ of each kink pair is just the sum of individual formation energies of the component defects, assuming that the two kinks are sufficiently widely separated that there is no interaction between them. The kink pairs plp–prp and nln–nrn are related by $\langle 110\rangle$ diad symmetry and therefore have the same formation energy ($E_{kp}^f = 1.04\,\text{eV}$). The remaining 14 kink pairs have calculated formation energies in the range 0.88–1.50 eV. The lowest-energy configuration is pln–nrn, although this kink pair requires a pre-existing pn APD state as the initial condition. The lowest-energy kink pair that can be formed from a perfect dislocation without a pre-existing APD is the pln–nrp pair. This pair has a formation energy of 0.96 eV, which is in close agreement with the empirical zero-stress activation enthalpy of 1.02 eV currently used in microscale dislocation dynamics simulations to model the temperature-dependent yield stress and plastic
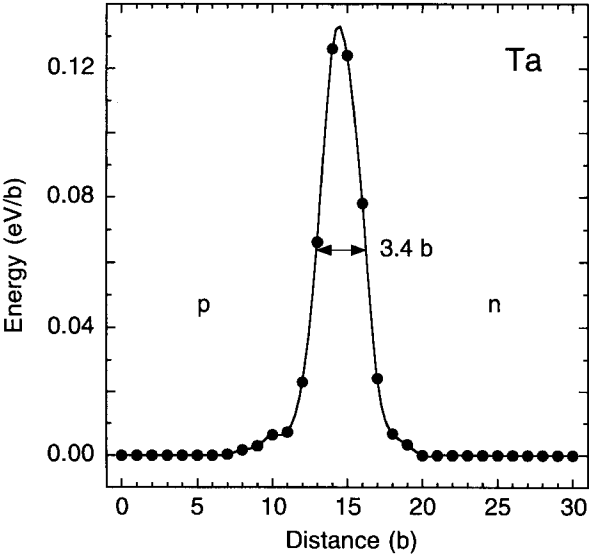


Figure 9.  Calculated energy profile of an isolated pln kink (●) in bcc Ta along a $\langle 111\rangle$ direction, as obtained from the present MGPT potentials. Each data point represents the energy difference between a unit disc containing the kink and one containing the rigid $(a/2)\langle 111\rangle$ screw dislocation. The half-width of the kink is seen to be 3.4*b*.

Table 6.   Total formation energies of 16 possible $(a/2)\langle 111\rangle$ screw dislocation kink pairs in bcc Ta, including configurations with the formation of an APD between the left and right kinks and/or an initial APD along the dislocation line, as required.

| Initial APD | Left kink | APD | Right kink | Formation Energy (eV) |
|---|---|---|---|---|
| | nn | | nn | 1.04 |
| np | nn | | np | 1.38 |
| | nn | np | pn | 1.47 |
| np | nn | np | pp | 1.50 |
| | pp | | pp | 1.04 |
| pn | pp | | pn | 1.27 |
| | pp | pn | np | 1.18 |
| pn | pp | pn | nn | 1.10 |
| | np | | pn | 1.32 |
| np | np | | pp | 1.35 |
| | np | pn | nn | 1.15 |
| np | np | pn | np | 1.47 |
| | pn | | np | 0.96 |
| pn | pn | | nn | 0.88 |
| | pn | np | pp | 1.08 |
| pn | pn | np | pn | 1.28 |

flow in bcc Ta (Tang *et al.* 1998, M. Tang 2000, private communication). At a sufficiently large separation, a kink pair may also be simulated together in a single simulation cell. Figure 10 shows the calculated energy profile of the pln–nrp kink pair positioned at a separation distance of $30b$ in a simulation cell of length $120b$. The asymmetry of the left- and right-hand kinks can be seen, with the nrp kink being wider and exhibiting a higher-energy profile than the pln kink.
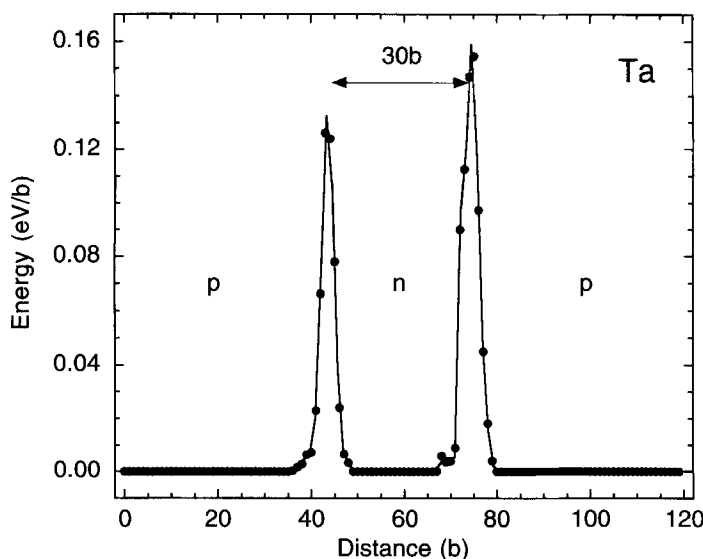


Figure 10.   Calculated energy profile of a pln–nrp kink pair in bcc Ta simulated in a single cell, as in figure 9 for the isolated pln kink. Note that the left kink has a lower formation energy and smaller width than the right kink.

At smaller finite separations, the left and right kinks will elastically attract each other, requiring an applied shear stress to maintain the separation, and yielding an interaction energy $E_{int}$ in addition to the large-separation formation energy $E_{kp}^f = E_l^f + E_r^f$. If the kink–kink separation $\lambda$ is much larger than the kink width (about $(5-10)b$ for Ta), linear elasticity can be used to estimate $E_{int}$. The total formation energy $E_{tot}^f$ of a kink pair can then be expressed as

$$E_{tot}^f = E_{kp}^f + E_{int} = E_l^f + E_r^f - \frac{k}{\lambda}, \qquad (16)$$

where $k$ is a geometrical pre-factor. During the kink-pair activation process, the energy required to generate the kink pair is supplied partly by thermal activation and partly by the work done by the applied shear stress needed to maintain the pair at separation distance $\lambda$. The stress-dependent activation enthalpy for such a balanced kink pair is given by

$$\Delta H(\tau) = E_{tot}^f - \tau \lambda h b. \qquad (17)$$

To investigate the relationships between $E_{tot}^f$ and the stress $\tau$, we have performed atomistic simulations of a kink pair under a finite applied shear stress, using a cylindrical simulation cell of radius $15b$ (for the atomistic region) and length $120b$. Figure 11 shows the energy–separation and stress–separation relationships for the pln–nrp kink pair. For large separations of about $20b$ the formation energy approaches the zero-stress value of $0.96\,eV$ asymptotically. At small separations, the energy decreases rapidly and the stress required to stabilize the kink pair increases sharply. At intermediate separations $10b \leqslant \lambda \leqslant 20b$, the interaction energy varies approximately as $\lambda^{-1}$, as expected, while the applied shear stress varies as $\lambda^{-1.5}$.
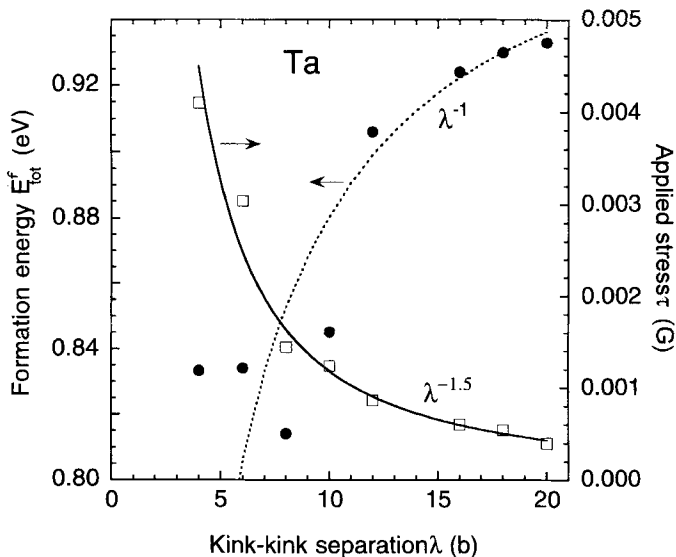
Figure 11.    The total stress-dependent kink-pair formation energy $E_{tot}^f$ ($\bullet$) and applied shear stress $\tau$ ($\square$) as functions of the kink–kink separation distance $\lambda$ for the pln–nrp pair in bcc Ta, as simulated with the present MGPT potentials; (——), (- - - -), approximate power-law fits to the calculated points.

The process of kink-pair formation is limited by the isolated kink formation energies. The competing process of kink migration is limited by the secondary Peierls stresses needed to move the left- and right-hand kinks. We have calculated the latter for the pln–nrp kink pair by applying a $\{110\}$–$\langle 111 \rangle$ shear stress separately to the isolated pln and nrp kinks. We find secondary Peierls stresses of $2.1 \times 10^{-4}G$ and $1.6 \times 10^{-3}G$ respectively, where $G = 62.5\,\text{GPa}$. These values are one to two orders of magnitude smaller than the corresponding Peierls stress for the rigid screw dislocation ($\tau_P = 1.0 \times 10^{-2}G$); so both kinks are expected to be mobile with the left kink moving faster than the right kink. Consequently, we expect the dislocation velocity at low stress to be controlled by kink-pair formation rather than by kink migration.

Finally, from the stress–separation ($\tau$–$\lambda$) and energy–separation ($E_{\text{tot}}^{\text{f}}$–$\lambda$) data shown in figure 11, it is possible to extract the activation enthalpy $\Delta H$ as a function of stress. This result is plotted in figure 12 as a function of $\tau/\tau_P$. For comparison, the empirical form currently used in dislocation dynamics simulations of single-crystal plasticity in bcc Ta (Tang *et al.* 1998),

$$\Delta H(\tau) = \Delta H(0)\left[1 - \left(\frac{\tau}{\tau_P}\right)^{0.748}\right]^{1.172}, \tag{18}$$

is also plotted, using the values $\Delta H(0) = 0.96\,\text{eV}$ and $\tau_P = 1.0 \times 10^{-2}G$ to normalize properly to the present pln–nrp kink-pair results. The agreement for $\tau/\tau_P \leqslant 0.2$ is clearly very good. Only the two higher-stress points calculated above $0.2\tau/\tau_P$, corresponding to kink–kink separations less than $7b$ in figure 11, are strongly deviating from equation (18). Clearly the implicit assumption of weakly interacting kinks in our calculation is breaking down in this regime, as is already apparent from figure
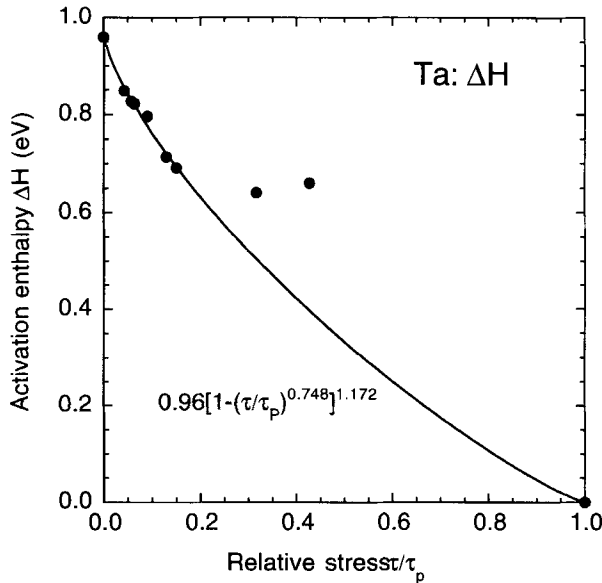


Figure 12.   Calculated activation enthalpy $\Delta H$ (●) as a function of relative applied stress $\tau/\tau_P$ for bcc Ta, as obtained from the data in figure 11 via equation (17): (———), one-parameter normalized fit to the calculated data of the empirical form currently used in dislocation dynamics simulations of Ta plasticity, as discussed in the text.

11. A full 3D atomistic calculation of double-kink formation and migration is needed at these higher stress levels (V. Vitek 2000, private communication).

### 4.3. *Peierls stress and its orientation dependence*

Finally, we turn to the high-stress limit and the calculation of the Peierls stress for the infinite rigid screw dislocation. In bcc metals, slip predominantly takes place in {110} and/or {112} planes at low temperatures but does not follow the well known Schmid law (Ito and Vitek 2001) and a rather complex orientation dependence of the slip geometry and the yield stress is experimentally observed (Takeuchi *et al.* 1972). Consequently, it is expected that there is a strong dependence of the critical resolved shear stress (CRSS) for the rigid $(a/2)\langle 111\rangle$ screw dislocation on the orientation of the applied stress and that this is the controlling factor for much of the observed behaviour (Duesbery 1984a, b, Duesbery and Vitek 1998, Ito and Vitek 2001).

The present 2D Peierls-stress simulations in bcc Ta were performed on the rigid $(a/2)\langle 111\rangle$ screw dislocation by applying either a pure glide shear stress or a shear with a uniaxial stress component on the relaxed core structure obtained from the 2D dislocation simulations described above. The CRSS is reached when the dislocation moves at least one lattice spacing on the maximum resolved shear stress (MRSS) plane. In order to determine the Peierls stress in a fully self-consistent manner, the present simulations have been performed at conditions of constant stress rather than constant volume or lattice parameter. A quasi-Newton method for continuously updating and optimizing the lattice parameter (Yang 1999) is used to maintain a constant external stress on the system. An iterative scheme is developed such that the internal and external degrees of freedom are optimized simultaneously. Whenever the lattice parameter changes, the volume-dependent MGPT potential parameters are redetermined, so that the correct interatomic interactions are maintained throughout the simulation.

In a bcc crystal along a given $\langle 111\rangle$ direction, there are three {110} planes and three {112} planes, mutually intersecting every 30°. Because of the twinning-anti-twinning asymmetry in the bcc lattice, unique values of the CRSS can exist on different planes ranging in orientation from $\chi = -30°$ (twinning orientation on {211}) to $\chi = 30°$ (antitwinning orientation on {211}), with $\chi$ being the angle measured from a given {110} slip plane. In this range, the CRSS in a bcc metal is expected to have a revealing orientation dependence under both pure shear and non-shear loading conditions (Duesbery 1984a, b, Ito and Vitek 2001). We have studied this orientation dependence in bcc Ta near ambient pressure for pure shear and selected uniaxial loadings on various MRSS planes. The calculated results are displayed in figure 13. As shown in the figure, the CRSS is indeed found to depend strongly on the orientation of the loading axis and for uniaxial loading the values are different in tension and compression. For pure shear loading, the CRSS is almost constant from $\chi = -30°$ to $\chi = 0°$ but then rises rapidly between 0° and 30°. The calculated CRSS ratio between $\chi = 30°$ and $\chi = -30°$ (antitwinning–twinning ratio) is 2.29. Our results also suggest a significant deviation from the Schmid law, for which the CRSS varies as $1/\cos(\chi + 30°)$ if the primary slip plane is along $\{\bar{1}\bar{1}2\}$ in the twinning sense in figure 13.

Our minimum calculated Peierls stress $\tau_p$ occurs for a pure shear stress with $\chi = -10°$ and has a magnitude of $9.4 \times 10^{-3}G = 590\,\mathrm{MPa}$. This value is a factor of about four smaller than calculated with simple FS potentials and fixed-boundary
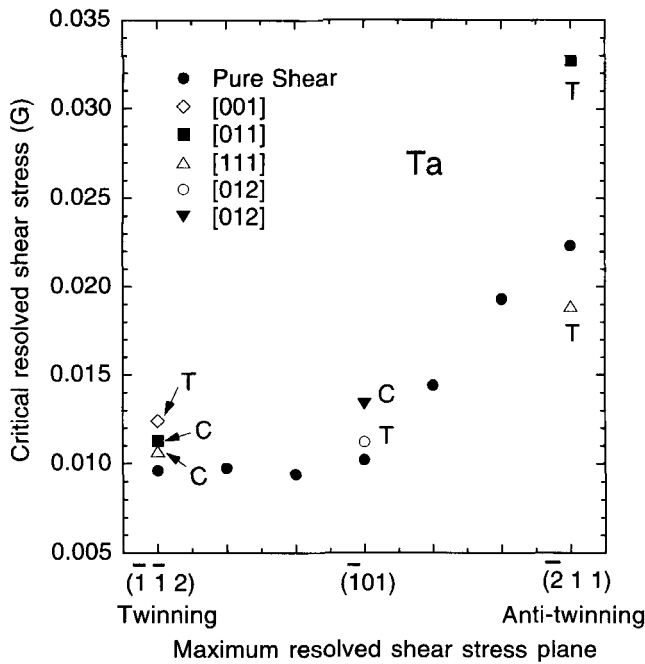
Figure 13. Calculated orientation dependence of the CRSS for a rigid $(a/2)\langle 111 \rangle$ screw dislocation in bcc Ta, as obtained with the present MGPT potentials. Stress orientations considered include both pure shear and shear plus a uniaxial stress component in either compression (C) or tension (T) for the indicated directions.

conditions for Ta at the same stress orientation (Ito and Vitek 2001). At the same time, our value is still a factor of about two larger than the best available empirical estimate under similar, although not identical stress orientation conditions (Lachenmann and Schultz 1970, Tang *et al.* 1998). The reasons for this latter disagreement are not clear at present, but there are several possibilities. On the experimental side, there is, of course, no direct measurement of the Peierls stress for an isolated dislocation, but only an inferred value obtained by extrapolating the temperature dependence of the yield stress for a deformed single crystal to zero temperature. On the theoretical side, the disagreement could reflect a limitation either in the present Ta MGPT potentials or in the method of simulation. With regard to the latter, our 2D zero-temperature calculation may possibly miss very-low-energy 3D and/or dynamic kink-like processes that would lead to an effectively lower Peierls stress. Such a mechanism has been argued to be operative in the case of edge dislocations for bcc metals (Duesbery and Xu 1998). In the future, we plan to perform 3D finite-temperature molecular dynamics simulations to investigate this possibility.

The glide path of the rigid screw dislocation motion has also been examined for an applied pure shear stress on the $(\bar{1}01)$ plane in the $\langle 111 \rangle$ direction. Prior work on the screw dislocation motion in bcc metals has shown that the core moves in atomic steps on $\{110\}$ planes, but that successive steps may be constrained to take place on either the same or different $\{110\}$ planes (Suzuki *et al.* 1991). In the former case, the preferred slip plane is $\{110\}$ and the unit translation is $(a/3)\langle 211 \rangle$. In the latter case, the dislocation moves in a zigzag pattern on successive $\{110\}$ planes, producing effective slip on a $\{211\}$ plane. The latter is the motion that we observe in Ta.

Mobile kink pairs of the degenerate screw core, however, can produce slip on either {110} or {211} planes. The creation of successive pln–nrp kink pairs will produce zigzag atomic motion on {110} planes as for the rigid screw dislocation and effective slip on {211} planes. The successive creation of plp–prp or nln–nrn kink pairs on the same {110} plane, on the other hand, will produce slip along that plane.

## § 5. CONCLUSIONS

In the present paper we have successfully developed and validated new MGPT many-body potentials in Ta and combined them with efficient 2D and 3D GF techniques and domain decomposition computational algorithms to simulate accurately the fundamental core properties of $(a/2)\langle 111 \rangle$ screw dislocations. Our rather extensive validation tests of a wide range of relevant deformations and defect properties suggest an approximate level of accuracy of 10–20% in such calculations, but confirmation of this expectation for the dislocation properties will still require substantial further work. We have predicted a weakly polarized and nearly isotropic core dislocation structure, but one that is subject to rapid change depending on the volume and pressure conditions considered. Our calculated kink and kink-pair properties in the low-stress limit appear to be quantitatively consistent with current mesoscale dislocation dynamics simulations of single-crystal plasticity and bode well for bridging the atomistic–mesoscale length-scale gap and providing fundamental input into those simulations. At the same time, in the high-stress limit there is still an apparent factor of two disagreement with regard to the magnitude of the Peierls stress that needs to be resolved. Even with that caveat, the calculated strong orientation dependence of the Peierls stress should be helpful in further investigating non-Schmid behaviour in the plasticity, as is currently being done with simpler FS potentials (Ito and Vitek 2001). Two important and related computational challenges for the future are to extend the calculation of kink-pair formation and migration to high stresses and to extend the 2D Peierls-stress calculations to 3D and to finite temperatures.

## REFERENCES

CAMPBELL, G. H., BELAK, J., and MORIARTY, J. A., 1999, *Acta mater.*, **47**, 3977; 2000, *Scripta mater.*, **43**, 659.
CAMPBELL, G. H., FOILES, S. M., GUMBSCH, P., RÜHLE, M., and KING, W. E., 1993, *Phys. Rev. lett.*, **70**, 449.
CARLSSON, A., 1990, *Solid St. Phys.*, **43**, 1; 1991, *Phys. Rev. B*, **44**, 6590.
DAW, M., and BASKES, M., 1983, *Phys. Rev. Lett.*, **50**, 1285.
DEDERICHS, P. H., and LEIBFRIED, G., 1969, *Phys. Rev.*, **188**, 1175.
DUESBERY, M. S., 1983a, *Acta metall.*, **31**, 1747; 1983b, *ibid.*, **31**, 1759; 1984a, *Proc. R. Soc. A*, **392**, 145; 1984b, *ibid.*, **392**, 175.
DUESBERY, M. S., and BASINSKI, Z. S., 1993, *Acta metall. mater.*, **41**, 643.
DUESBERY, M. S., and VITEK, V., 1998, *Acta mater.*, **46**, 1481.

DUESBERY, M. S., VITEK, V., and BOWEN, D., 1973, *Proc. R. Soc.* A, **332**, 85.

DUESBERY, M. S., and XU, W., 1998, *Scripta mater.*, **39**, 283.

FINNIS, M., and SINCLAIR, J., 1984, *Phil. Mag.* A, **50**, 45.

FOILES, S. M., 1993, *Phys. Rev.* B, **48**, 4287.

HARDER, J. M., and BACON, D. J., 1986, *Phil. Mag.* A, **54**, 651.

HIRSCH, P. B., 1960, *Proceedings of the Fifth International Conference on Crystallography* (Cambridge University Press), p. 139.

HOHENBERG, P., and KOHN, W., 1964, *Phys. Rev.*, **136**, B864.

ISMAIL-BEIGI, S., and ARIAS, T. A., 2000, *Phys. Rev. Lett.*, **84**, 1499.

ITO, K., and VITEK, V., 2001, *Phil. Mag.* A, **81**, 1387.

KATAHARA, K. W., MANGHNANI, M. H., and FISHER, E. S., 1979, *J. Phys.* F, **9**, 773.

KITTEL, C., 1976, *Introduction to Solid State Physics*, fifth edition (New York: Wiley), p. 74.

KOHN, W., and SHAM, L., 1965, *Phys. Rev.*, **140**, A1133.

LACHENMANN, R., and SCHULTZ, H., 1970, *Scripta metall.*, **4**, 709.

MORIARTY, J. A., 1988, *Phys. Rev.* B, **38**, 3199; 1990a, *ibid.*, **42**, 1609; 1990b, *Many-atom Interactions in Solids* (Berlin: Springer), p. 158; 1994, *Phys. Rev.* B, **49**, 12431.

MORIARTY, J. A., and SÖDERLIND, P., 2001, *Phys. Rev.* B (to be published).

MORRIS, J. W., JR, KRENN, C. R., ROUNDY, D., and COHEN, M. L., 2000, *Phase Transformations and Evolution in Materials*, edited by P. E. Turchi, and A. Gonis (Warrendale, Pennsylvania: Metallurgical Society of AIME).

OCHS, T., ELSÄSSER, C., MROVEC, M., VITEK, V., BELAK, J., and MORIARTY, J. A., 2000, *Phil. Mag.* A, **80**, 2405.

PATUKHOV, B., 1983, *Phys. Metals Metallogr. (USSR)*, **56**, 123.

PAXTON, A. T., GUMBSCH, P., and METHFESSEL, M., 1991, *Phil. Mag. Lett.*, **63**, 267.

PERDEW, J., CHEVARY, J., VOSKO, S., JACKSON, K., PEDERSON, M., and SINGH, D., 1992, *Phys. Rev.* B, **46**, 6671.

PETTIFOR, D. G., AOKI, M., GUMBSCH, P., HORSFIELD, A. P., NGUYEN-MANH, D., and VITEK, V., 1995, *Mater. Sci. Engng*, **A192–A193**, 24.

PINES, D., and NOZIÈRES, P., 1966, *The Theory of Quantum Liquids* (New York: Benjamin).

RAO, S., HERNANDEZ, C., SIMMONS, J., PARTHASARATHY, T., and WOODWARD, C., 1998, *Phil. Mag.* A, **77**, 231.

RAO, S., and WOODWARD, C., 2001, *Phil. Mag.* A, **81**, 1317.

SCHULTZ, H., and EHRHART, P., 1991, *Atomic Defects in Metals*, (Berlin: Springer).

SEEGER, A., and WÜTHRICH, C., 1976, *Nuovo Cim.* B, **33**, 38.

SINCLAIR, J., GEHLEN, P., HOAGLAND, R., and HIRTH, J., 1978, *J. appl. Phys.*, **49**, 3890.

SÖDERLIND, P. and MORIARTY, J. A., 1998, *Phys. Rev.* B, **57**, 10340.

SÖDERLIND, P., YANG, L. H., MORIARTY, J. A., and WILLS, J. M., 2000, *Phys. Rev.* B, **61**, 2579.

STROH, A. N., 1958, *Phil. Mag.*, **3**, 625; 1962, *J. math. Phys.*, **41**, 77.

SUZUKI, T., TAKEUCHI, S., and YOSHINAGA, H., 1991, *Dislocation Dynamics and Plasticity* (Berlin: Springer).

TAKEUCHI, S., KURAMOTO, E., and SUZUKI, T., 1972, *Acta metall.*, **20**, 909.

TANG, M., KUBIN, L. P., and CANOVA, G. R., 1998, *Acta mater.*, **46**, 3221.

VITEK, V., 1974, *Cryst. Lattice Defects*, **5**, 1; *Proc. R. Soc.* A, **352**, 85.

WOODS, A. D. B., 1964, *Phys. Rev.*, **136**, A781.

XU, W., and MORIARTY, J. A., 1996, *Phys. Rev.* B, **54**, 6941; 1998, *Comput. Mater. Sci.*, **9**, 348.

YANG, L. H., 1999, *Industrial Strength Parallel Computing* (San Francisco, California: Morgan Kaufmann), p. 297.

YANG, L. H., and MORIARTY, J. A., 2000, *Mater. Sci. Engng*, A (to be published); 2001, *Comput. Phys. Commun.* (to be published).

YANG, L. H., SÖDERLIND, P., and MORIARTY, J. A., 2000, *Mater. Sci. Engng*, A (to be published); 2001 (to be be published).